Universal growth of magnetic energy during the nonlinear phase of subsonic and supersonic small-scale dynamos

Neco Kriel,* Mark R. Krumholz, and Patrick J. Armstrong
Research School of Astronomy and Astrophysics, Australian National University, 233 Mount Stromlo Road, Stromlo, Austrailian Capital Territory 2612, Australia

James R. Beattie†
Canadian Institute for Theoretical Astrophysics, University of Toronto, Toronto, Ontario, Canada M5S3H8 and Department of Astrophysical Sciences, Princeton University, Princeton, New Jersey 08540, USA

Jennifer Schober
Argelander-Institut für Astronomie, Universität Bonn, Auf dem Hügel 71, 53121 Bonn, Germany

(Received 12 September 2025; accepted 23 February 2026; published 10 April 2026)

Small-scale dynamos (SSDs) amplify magnetic fields in turbulent plasmas. Theory predicts nonlinear magnetic energy growth $E_{\rm mag} \propto t^{p_{\rm nl}}$, but this scaling has not been tested across flow regimes. Using a large ensemble of SSD simulations spanning subsonic to supersonic turbulence, we measure linear growth ($p_{\rm nl} = 1$) in subsonic flows and quadratic growth ($p_{\rm nl} = 2$) in supersonic flows. In all cases, the nonlinear dynamo converts a nearly constant fraction approximately equal to $1/100$ of the turbulent kinetic energy flux into magnetic energy, and the nonlinear phase has a characteristic duration $\Delta t \approx 20\, t_0$, where t_0 is the outer-scale turnover time. By isolating the onset of magnetic backreaction in SSDs, our statistical ensemble approach identifies a robust efficiency and duration for the nonlinear SSD that can be used to interpret more complex astrophysical and laboratory plasmas.

DOI: 10.1103/8qjf-8gg4

I. INTRODUCTION

Small-scale dynamo (SSD) action describes the process by which motions in a plasma with dynamically weak magnetic fields amplify and then maintain the magnetic energy density $E_{\rm mag}$ to levels comparable to the turbulent kinetic energy density $E_{\rm kin}$ [1–3]. This process is ubiquitous across astrophysical, geophysical, and laboratory environments, both those where the plasma supports turbulent subsonic motions (turbulent sonic Mach number $\mathcal{M} = u_0/c_s < 1$, where u_0 is the rest-frame root-mean-square velocity and c_s the sound speed) and those where the motions are supersonic ($\mathcal{M} > 1$). The fields generated in this process magnetize the plasma between galaxies [4,5], provide pressure support against collapse in galaxy mergers [6], enable rapid spin down of stellar merger remnants [7,8], and modify cosmic ray propagation via curvature acceleration in the interstellar medium [9,10]. Direct evidence for SSD action comes both from *in situ* observations in the earth's subsonic magnetosheath [11] and from supersonic laboratory laser experiments [12–15].

Small-scale dynamos evolve through a number of distinct phases [2,16–21]. At first the magnetic field is too weak to exert significant forces on the plasma and thus the velocity field is kinematic, which leads to exponential amplification of the magnetic energy density $E_{\rm mag} \propto \exp(\gamma_{\rm exp} t)$. Here $\gamma_{\rm exp}$ is the kinematic growth rate (with units of inverse time) and the dimensionless product $\gamma_{\rm exp} t_0$ measures how efficiently kinetic energy is converted into magnetic energy over one outer-scale eddy turnover time $t_0 = \ell_0/u_0$, where u_0 is the flow velocity on the outer scale ℓ_0 [16,18]. For magnetic Prandtl numbers ${\rm Pm} \gtrsim 1$, the dimensionless growth rate is predicted to scale as $\gamma_{\rm exp} t_0 \propto {\rm Re}^{1/2}$ for $\mathcal{M} < 1$ and $\gamma_{\rm exp} t_0 \propto {\rm Re}^{1/3}$ for $\mathcal{M} > 1$, where ${\rm Re} \sim u_0 \ell_0/\nu$ is the hydrodynamic Reynolds number [22] and ν is the kinematic viscosity. Field amplification is driven by chaotic stretching [2], which occurs on an eddy turnover timescale $t_\ell \sim \ell/u_\ell$, where u_ℓ is the flow speed on size scale ℓ and thus is fastest on the viscous scale ℓ_ν, which, for Kolmogorov turbulence, is the scale on which eddies evolve on the shortest timescales [23–28]. However, once the kinematic dynamo amplifies the field such that $E_{\rm mag} \approx E_{\rm kin}$ on scale ℓ_ν, the magnetic field begins to back react on the velocity, marking the end of the kinematic phase and the start of the nonlinear phase. During this phase the dominant stretching scale ℓ_s shifts to larger ℓ with longer t_ℓ, driving a slower, secular dynamo. As the field grows, it suppresses stretching on ever-larger scales, until ℓ_s reaches a maximum scale. At this point the dynamo reaches the saturated phase and becomes statistically steady, driven MHD turbulence [29].

Both numerical simulations [20,26,27] and laboratory experiments [13–15] confirm that the evolution of $E_{\rm mag}$ during the kinematic phase agrees well with both the SSD theory of Kazanstev [30] and Kulsrud and Anderson [18] and numerical works in the $\mathcal{M} > 1$ regime [27,31,32]. However, this well-understood phase likely ends almost immediately in

*Contact author: neco.kriel@anu.edu.au
†Contact author: james.beattie@princeton.edu

real astrophysical plasmas. This is because the growth rate is $\gamma_{\rm exp} t_0 \propto {\rm Re}^{1/2}$, and many warm or cold astrophysical plasmas, at least in our galaxy and its surrounding medium, often have ${\rm Re} \sim 10^3$–10^{10}, thus making the kinematic phase persist for only a small fraction of the outer dynamical timescale. Hence, almost any observable astrophysical system where the field is growing will instead be in the nonlinear phase, which is a regime that has not yet been explored with the same level of numerical detail as the kinematic dynamo.

While there is indication that the nonlinear phase yields secular growth for the magnetic energy [27,33–36] $E_{\rm mag} = \alpha_{\rm nl} t^{p_{\rm nl}}$, there are no simulations to date that have measured the efficiency $\alpha_{\rm nl}$ and growth order $p_{\rm nl}$ across a wide range of plasma Reynolds number Re and Mach number $\mathcal{M}$. For incompressible Kolmogorov-like turbulence, where $E_{\rm kin}(\ell) \propto \ell^{5/3}$, the prevailing expectation and hint from numerical simulations is that $p_{\rm nl} = 1$ [18,19,33,34,37] and $\alpha_{\rm nl} \propto \varepsilon$, where $\varepsilon \sim \rho_\ell u_\ell^3/\ell$ is the turbulent energy flux through scale ℓ, with ρ_ℓ the density associated with motions on that scale (which is constant in the incompressible limit). In contrast, for highly compressible, shock-dominated turbulence, where $E_{\rm kin}(\ell) \propto \ell^2$ (as in Burgers-like turbulence [27,28,38,39]), the outcome is debated: Some models [40,41] predict quadratic growth ($p_{\rm nl} = 2$), while others suggest universal linear growth ($p_{\rm nl} = 1$) [33].

This lack of consensus about the nonlinear growth order $p_{\rm nl}$ and efficiency $\alpha_{\rm nl}$, particularly in highly compressible turbulence, is largely due to a dearth of numerical and experimental guidance, which is missing in large part because it is extremely challenging to accurately measure the nonlinear phase. At the modest values of Re accessible to numerical simulations and laboratory experiments, the nonlinear phase is hard to identify, due in part to the strong fluctuations of integral quantities that can easily mask underlying trends, especially in supersonic flows. Our goal in this study is to take on these challenges by focusing on plasmas with ${\rm Pm} = 1$ for which the nonlinear phase we resolve can only be the backreaction stage that begins once $E_{\rm mag} \approx E_{\rm kin}$ on the viscous scale. This choice also maximizes the computational dynamic range over which the nonlinear backreaction can operate, because the viscous and resistive dissipation scales for any choice of Re or Rm coincide with one another ($\ell_\nu \approx \ell_\eta$). Within this setting we directly measure $\alpha_{\rm nl}$ and $p_{\rm nl}$ across a broad range of plasma parameters (in Re and $\mathcal{M}$), allowing us to confront theoretical predictions for the backreaction during the nonlinear phase with highly detailed measurements from simulations. At the same time, our results provide a well-controlled reference point for future studies of more realistic hot astrophysical plasmas with ${\rm Pm} \gg 1$, where this backreaction stage may be preceded by an additional nonlinear, secular growth phase in the subviscous range (see the discussion in the Conclusion).

II. NUMERICAL METHODS

A. Numerical simulations

We used a modified version of the FLASH code [39,42–44] to run a series of direct numerical simulations that solve the compressible, nonideal MHD equations for an isothermal plasma in a three-dimensional periodic box [27]; the full set of equations we solve is provided in Appendixes A–C. We work in dimensionless units where the box size L, mean density ρ_0, c_s, and mean thermal energy $\rho_0 c_s^2$ are unity. The natural unit of time for this system is the sound-crossing time $t_{\rm sc} = L/c_s = 1$ and the turbulent velocity u_0 directly sets the sonic Mach number $\mathcal{M} = u_0/c_s$. By varying u_0, we control the speed of the flow relative to $t_{\rm sc}$ and in turn can explore subsonic ($t_{\rm sc} < t_0$) and supersonic ($t_0 < t_{\rm sc}$) regimes. We use the TURBGEN [45] forcing module to drive purely solenoidal ($\boldsymbol{\nabla} \cdot \boldsymbol{f} = 0$) turbulence with momentum source term $\boldsymbol{f}$, following the standard protocol outlined in Ref. [26], allowing us to set $\mathcal{M} \in [5 \times 10^{-2}, 5]$ (see the Appendixes for more details).

By varying the (constant in space and time) kinematic viscosity coefficient ν across different simulation configurations, we explore a range of hydrodynamic Reynolds numbers ${\rm Re} \in [10^3, 5 \times 10^3]$, where we set the magnetic Prandtl number ${\rm Pm} \equiv \nu/\eta = {\rm Rm}/{\rm Re} = 1$; η is the magnetic resistivity coefficient and Rm is the magnetic Reynolds number. We quote Re and Rm using u_0, which is the rest-frame root-mean-square velocity measured in the statistically steady kinematic phase. For convenience, we use these kinematic values to label simulations and compare across the parameter space. During the nonlinear and saturated phases, magnetic backreaction slightly suppresses the velocity amplitude, so the instantaneous effective values of Re and Rm may be smaller than their nominal kinematic values. This effect, however, is minor for ${\rm Pm} = 1$, becoming more prominent for ${\rm Pm} \gg 1$ [46,47]. Because ${\rm Re} = {\rm Rm} \gtrsim {\rm Rm}_{\rm crit} \approx 100$, all simulations are above the critical Rm required to undergo all phases of the SSD [41,48,49]. In total we consider 12 distinct (but over many different statistical realizations of $\boldsymbol{f}$, detailed in the next paragraph) combinations of $\mathcal{M}$ and Re; see the Appendixes for a complete list of simulations. We also ran pilot simulations at lower Re, but found that the volume-integrated kinetic and magnetic energies had relative fluctuations that were too large for our analysis. When the viscous and resistive dissipation scales ℓ_ν and ℓ_η lie close to the forcing scale ℓ_0, the cascade is truncated and fluctuations remain confined to large scales. The effective number of independent eddies contributing to volume averages, $N_{\rm eddies} \sim (L/\ell_\nu)^3$, is then small, so the fractional fluctuations proportional to $N_{\rm eddies}^{-1/2}$ remain large in the nonlinear phase. For this reason we adopt moderately turbulent flows with ${\rm Re} \gtrsim 10^3$ as our practical lower bound. Finally, we caution readers that there are two different conventions in use in the literature to define the Reynolds number; our definition ${\rm Re} \sim u_0 \ell_0/\nu$ is a factor of 2π larger than that used by some authors (see, e.g., [36,50]), so in the convention used by these authors, our simulations span ${\rm Re} \in [1.5 \times 10^2, 8 \times 10^2]$.

In all our simulations we initialize a weak seed magnetic field $E_{\rm mag,0} \equiv E_{\rm mag}(t = 0) = 10^{-10} E_{\rm kin}$, where $E_{\rm kin}$ is the kinetic energy once turbulence is fully established in the kinematic phase. We evolve each simulation instance long enough to unambiguously identify the onset and transition out of the nonlinear phase (see the next section). To reduce the impact of fluctuations during the nonlinear phase on our fit parameters, we repeat each configuration at least five times with different random seeds for $\boldsymbol{f}$. We perform runs at three

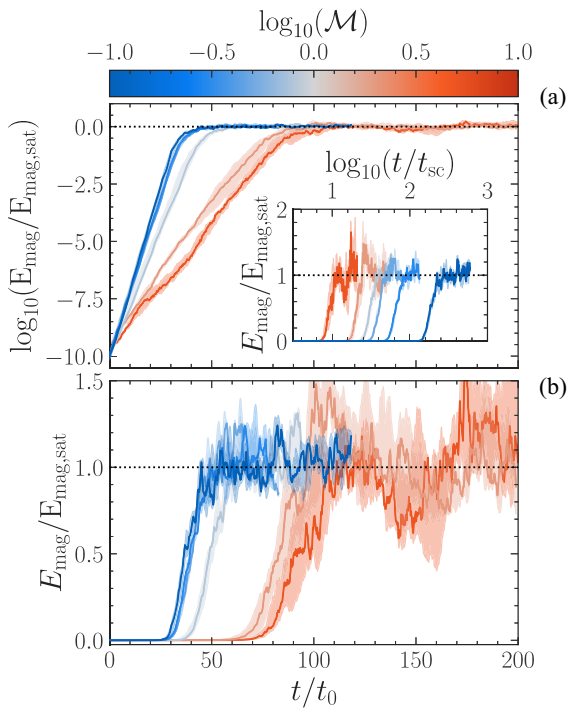

FIG. 1. Time evolution of the volume-averaged magnetic energy $E_{\rm mag}$, normalized by the final saturated value $E_{\rm mag,sat}$, for a subset of SSD simulations with Re = 1500 and the energy in (a) logarithmic scale and (b) (and inset) linear scale. Each simulation configuration is repeated five times with independent random seeds for the turbulent forcing; we plot the median trend across realizations as a solid line, with the 16th to 84th percentile range indicated by a shaded band. Colors indicate the average sonic Mach number $\mathcal{M}$ of each configuration. Time is shown in units of the turbulent turnover time on the outer scale t_0 on the main axes and rescaled to the sound-crossing time $t_{\rm sc}$ in the inset.

resolutions $N_{\rm res} \in \{288^3, 576^3, 1152^3\}$ and run a total of 89 independent simulation instances. We plot the time evolution for the integral magnetic field energy of a representative subset of our simulations ($\mathcal{M}$ varied with Re = 1500) in Fig. 1, where the classical SSD phases are clear to see. The main panels use t_0 to emphasize the evolution in outer-scale turnover times, while the inset renormalizes the same curves in units of the sound-crossing time $t_{\rm sc}$, highlighting how the ordering of the nonlinear phase onset changes when measured against $t_{\rm sc}$ rather than t_0.

B. Fitting procedure

To constrain growth timescales during the nonlinear phase, we begin by binning the raw time series of volume-averaged magnetic energy density $E_{\rm mag}$, for each of our simulations, into intervals of t_0. Within each time bin t_i, we compute the mean μ_i and standard deviation σ_i of both $E_{\rm mag}$ and $\ln(E_{\rm mag})$ in bin i; $\mu_i^{(\ln)}$ and $\sigma_i^{(\ln)}$ indicate the mean and standard deviation of $\ln(E_{\rm mag})$ in bin i. This yields, for each simulation j, a dataset $\mathcal{D}_j \equiv (t_i, \mu_i, \mu_i^{(\ln)}, \sigma_i, \sigma_i^{(\ln)})$, where data points are (approximately) uncorrelated, given that the turbulence correlation time is t_0.

Using a hierarchical two-stage strategy, we then employ a Bayesian approach to fit each $\mathcal{D}_j$ to models for the time evolution of magnetic energy. In the first stage we only constrain the exponential and saturated behavior, and in the second stage we fit the full three-phase model with priors informed by the first. This ensures that the more complex nonlinear-phase dynamics remains stable and well constrained, especially in our supersonic simulations, where large fluctuations can make the nonlinear phase difficult to identify. Anchoring in this way also improves the sampling efficiency.

Our first stage models only the kinematic and saturated phases, approximating the transition between these phases as instantaneous,

$$f_1(t \mid \boldsymbol{\theta}_1) = \begin{cases} E_0 \exp(\gamma_{\rm exp} t), & t < t_{\rm sat} \\ E_0 \exp(\gamma_{\rm exp} t_{\rm sat}), & t \geqslant t_{\rm sat}, \end{cases} \tag{1}$$

with $\boldsymbol{\theta}_1 = (E_0, \gamma_{\rm exp}, t_{\rm sat})$, and the second stage models all dynamo phases self-consistently as

$$f_2(t \mid \boldsymbol{\theta}_2) = \begin{cases} E_0 \exp(\gamma_{\rm exp} t), & t < t_{\rm nl} \\ E_0 \exp(\gamma_{\rm exp} t_{\rm nl}) + \alpha_{\rm nl}(t - t_{\rm nl})^{p_{\rm nl}}, & t_{\rm nl} \leqslant t < t_{\rm sat} \\ E_{\rm sat}, & t \geqslant t_{\rm sat}, \end{cases} \tag{2}$$

where $\boldsymbol{\theta}_2 = (E_0, E_{\rm sat}, \gamma_{\rm exp}, t_{\rm nl}, t_{\rm sat}, p_{\rm nl})$. Here $\alpha_{\rm nl}$ is not a fit parameter in the second stage, because it is implicitly set by the requirement that f_2 must remain continuous at $t = t_{\rm sat}$.

For our fits in both stages, we assume that each data point d_i in the time series is an independent sample from a Gaussian distribution around a mean trend, so for any given time series of simulation data $\mathcal{D}_j$, the log-likelihood function is

$$\ln \mathcal{L}(\boldsymbol{\theta}_s \mid \mathcal{D}_j) = -\frac{1}{2} \sum_i \left(\frac{[d_i - f_s(t_i \mid \boldsymbol{\theta}_s)]^2}{e_i^2} \right), \tag{3}$$

where we fit $(d_i, e_i) = (\mu_i^{(\ln)}, \sigma_i^{(\ln)})$ in stage 1 ($s = 1$) and we fit $(d_i, e_i) = (\mu_i, \sigma_i)$ in stage 2 ($s = 2$). This is because, as is apparent from Fig. 1, it is much easier to identify the kinematic (exponential growing) phase in logarithmic space and the nonlinear (backreaction) phase in linear space.

We fit using a Markov chain Monte Carlo method (MCMC) [51]; see Appendix B for details on our sampling parameters. In the first stage we adopt uniform (unbiased) priors on $\gamma_{\rm exp} \in (0, 10]$ and $t_{\rm sat} \in (0, t_{\rm end})$, where $t_{\rm end}$ is the final time bin, and a log-uniform prior on $E_0 \in [10^{-30}, 10^{-5}]$ (due to its wide dynamic range). In the second stage, the priors for E_0, $\gamma_{\rm exp}$, and $E_{\rm sat}$ are taken to be the posteriors from stage 1. We assign a uniform prior $p_{\rm nl} \in [1, 2]$, consistent with existing theories, while for $t_{\rm nl}$ and $t_{\rm sat}$ we use priors that are uniform on the intervals $[0, t_{\rm nl,max}]$ and $[t_{\rm nl}, t_{\rm sat,max}]$, where $t_{\rm nl,max}$ is the time bin where $dE_{\rm mag}/dt$ is its maximum, and $t_{\rm sat,max}$ is the earliest time t_i for which $dE_{\rm mag}/dt < 0$.

After fitting each individual simulation, we aggregate posteriors across runs with the same resolution and plasma parameters. This is the key step in our procedure, where we average out the inevitably large fluctuations in any single realization. For a given configuration, all realizations are statistically equivalent and differ only in their random driving, so we combine their posterior samples with equal weighting.

TABLE I. Summary of simulation configurations. Columns 1–3 list key plasma parameters, column 4 lists the number of instances at a particular resolution, and columns 5–8 list the dimensionless parameters inferred from our MCMC fitting routine for the ensemble-averaged runs at the respective resolution. Note that we report columns 5–8 in dimensionless units.

$\mathcal{M}$	Re	$\nu t_0/\ell_0^2$	Runs	$\gamma_{\rm exp} t_0$	$\alpha_{\rm nl}$	$p_{\rm nl}$	$(t_{\rm sat}-t_{\rm nl})/t_0$
0.05	1500	1.7×10^{-5}	5×288	$1.1^{+0.1}_{-0.1}$	$(1.8^{+0.7}_{-0.4})\times10^{-6}$	$1.1^{+0.8}_{-0.1}$	$16.2^{+3.1}_{-7.7}$
0.05	1500	1.7×10^{-5}	5×576	$1.2^{+0.1}_{-0.1}$	$(1.7^{+0.6}_{-0.5})\times10^{-6}$	$1.4^{+0.4}_{-0.4}$	$16.0^{+6.1}_{-5.4}$
0.1	1500	3.3×10^{-5}	5×576	$1.26^{+0.05}_{-0.07}$	$(1.0^{+0.5}_{-0.3})\times10^{-5}$	$1.0^{+0.7}_{-0.1}$	$18.5^{+5.5}_{-5.9}$
0.3	1500	1×10^{-4}	1×288	$1.3^{+0.1}_{-0.1}$	$(2.22^{+0.02}_{-0.02})\times10^{-4}$	$1.22^{+0.03}_{-0.03}$	$16.5^{+0.3}_{-0.2}$
0.3	1500	1×10^{-4}	1×576	$1.2^{+0.1}_{-0.1}$	$(1.82^{+0.01}_{-0.01})\times10^{-4}$	$1.0^{+0.1}_{-0.1}$	$19.0^{+0.1}_{-0.1}$
0.3	1500	1×10^{-4}	3×1152	$1.30^{+0.01}_{-0.02}$	$(2.6^{+0.4}_{-0.4})\times10^{-4}$	$1.00^{+0.01}_{-0.10}$	$14.3^{+5.1}_{-0.3}$
0.5	1000	2.5×10^{-4}	9×576	$(9.5^{+0.3}_{-0.4})\times10^{-1}$	$(9^{+5}_{-2})\times10^{-4}$	$1.1^{+0.9}_{-0.1}$	$24.3^{+8.5}_{-11.8}$
0.5	1500	1.7×10^{-4}	6×576	$1.3^{+0.2}_{-0.1}$	$(0.7^{+0.2}_{-0.6})\times10^{-3}$	$1.1^{+0.5}_{-0.1}$	$14.9^{+5.4}_{-4.5}$
0.5	1500	1.7×10^{-4}	3×1152	$1.26^{+0.06}_{-0.04}$	$(1.3^{+0.4}_{-0.1})\times10^{-3}$	$1.3^{+0.6}_{-0.3}$	$12.7^{+2.3}_{-2.8}$
0.5	3000	8.3×10^{-5}	9×576	$1.8^{+0.1}_{-0.2}$	$(1.3^{+0.2}_{-0.1})\times10^{-3}$	$1.0^{+0.2}_{-0.1}$	$16.6^{+3.6}_{-2.2}$
0.5	3000	8.3×10^{-5}	3×1152	$1.9^{+0.2}_{-0.1}$	$(1.0^{+0.2}_{-0.1})\times10^{-3}$	$1.08^{+0.10}_{-0.08}$	$17.3^{+0.9}_{-3.0}$
0.5	5000	5×10^{-5}	1×576	$2.42^{+0.01}_{-0.01}$	$(1.73^{+0.02}_{-0.01})\times10^{-3}$	$1.22^{+0.03}_{-0.03}$	$16.5^{+0.2}_{-0.2}$
0.5	5000	5×10^{-5}	5×1152	$2.4^{+0.2}_{-0.3}$	$(1.7^{+0.4}_{-0.3})\times10^{-3}$	$1.1^{+0.2}_{-0.1}$	$16.7^{+1.3}_{-4.3}$
0.8	1500	2.7×10^{-4}	1×288	$1.1^{+0.1}_{-0.1}$	$(3.06^{+0.05}_{-0.04})\times10^{-3}$	$1.22^{+0.02}_{-0.02}$	$14.0^{+0.2}_{-0.3}$
0.8	1500	2.7×10^{-4}	1×576	$(9.9^{+0.1}_{-0.1})\times10^{-1}$	$(2.40^{+0.01}_{-0.01})\times10^{-3}$	$1.03^{+0.01}_{-0.01}$	$23.6^{+0.1}_{-0.1}$
0.8	1500	2.7×10^{-4}	3×1152	$1.1^{+0.1}_{-0.1}$	$(4^{+1}_{-1})\times10^{-3}$	$1.5^{+0.4}_{-0.5}$	$17.0^{+0.3}_{-1.0}$
2.0	1500	6.7×10^{-4}	5×576	$(5.1^{+0.8}_{-0.6})\times10^{-1}$	$(2.3^{+0.2}_{-0.4})\times10^{-2}$	$1.8^{+0.2}_{-0.8}$	$25.9^{+2.2}_{-2.6}$
2.0	3000	3.3×10^{-4}	5×288	$(7^{+1}_{-1})\times10^{-1}$	$(2^{+2}_{-1})\times10^{-2}$	$1.6^{+0.3}_{-0.5}$	$28.7^{+9.3}_{-13.8}$
5.0	1500	1.7×10^{-3}	5×576	$(5.3^{+0.3}_{-0.5})\times10^{-1}$	$(1.1^{+0.5}_{-0.3})\times10^{-1}$	$1.8^{+0.2}_{-0.6}$	$21.5^{+18.4}_{-1.5}$
5.0	3000	8.3×10^{-4}	5×576	$(6.7^{+0.2}_{-0.3})\times10^{-1}$	$(2^{+1}_{-1})\times10^{-1}$	$1.9^{+0.1}_{-0.8}$	$17.0^{+10.4}_{-5.7}$
5.0	5000	5×10^{-4}	5×576	$(7.3^{+0.7}_{-0.3})\times10^{-1}$	$(2^{+2}_{-1})\times10^{-1}$	$1.6^{+0.4}_{-0.4}$	$22.3^{+12.8}_{-6.8}$

Fitting each simulation separately preserves the phase structure of each realization while still averaging over ensemble variability. This is crucial, because identical realizations may enter the nonlinear and saturated phases at slightly different times relative to one another. Accurately constraining these transition times is essential for robustly measuring the nonlinear growth dynamics, which would be averaged out if all instances of a configuration were fit simultaneously. All the results we present in the remainder of this study are derived from these aggregated samples; percentiles of these derived quantities are reported in Table I, and the raw data, along with our implementation of the routines discussed here, are publicly available online [52].

III. RESULTS

A. Kinematic dynamo growth

In Fig. 2 we show our inferred kinematic-phase growth rates $\gamma_{\rm exp} t_0$ for each plasma configuration. Consistent with both theoretical expectation and prior work, we find that the data follow $\gamma_{\rm exp} \propto {\rm Re}^{1/2}$ for $\mathcal{M} \lesssim 1$ and $\gamma_{\rm exp} \propto {\rm Re}^{1/3}$ for $\mathcal{M} > 1$ simulations. Both scalings align with the expectation that magnetic growth is regulated by the stretching on the viscous scale of the hydrodynamical cascade, $\gamma_{\rm exp} \sim u_\nu/\ell_\nu \sim {\rm Re}^{(1-\vartheta)/(1+\vartheta)}$, with $\vartheta = 1/2$ for Kolmogorov-like and $\vartheta = 1/3$ for Burgers-like turbulence [18,19,22]. We find that the growth rate transitions sharply between the two regimes, i.e., as soon as the turbulence becomes even mildly supersonic the growth rate follows $\gamma_{\rm exp} \propto {\rm Re}^{1/3}$.

While the scaling of $\gamma_{\rm exp}$ with Re in our simulations is in agreement with theoretical expectations, the proportionality constants we measure, of order of approxiately $1/100$, are systematically smaller than expected. A simple least-squares fit of the dimensionless kinematic growth rate $\gamma_{\rm exp} t_0$ as a function of Re gives $(3.22 \pm 0.06) \times 10^{-2}\,{\rm Re}^{1/2}$ for our $\mathcal{M} \lesssim 1$ simulations and $(4.48 \pm 0.06) \times 10^{-2}\,{\rm Re}^{1/3}$ for our

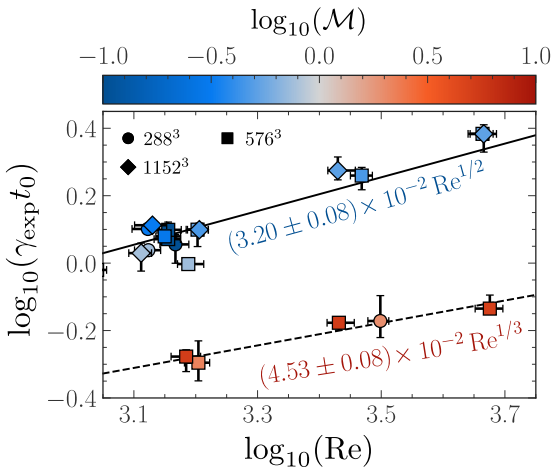

FIG. 2. Kinematic growth rate $\gamma_{\rm exp}$ as a function of plasma Reynolds number Re, with markers indicating different $N_{\rm res}$ and colors showing $\mathcal{M}$. Each data point shows the median marginal posterior probability for $\gamma_{\rm exp}$ derived by fitting Eq. (2) to each plasma combination ($N_{\rm res}$, $\mathcal{M}$, Re). The vertical error bars show the 16th to 84th percentile range from the fits and the horizontal error bars show the same for the fluctuation measure in ${\rm Re} = u_0 \ell_0/\nu$ over time. Lines show fits of $\gamma_{\rm exp} \propto {\rm Re}^{1/2}$ to subsonic points (solid line) and $\gamma_{\rm exp} \propto {\rm Re}^{1/3}$ to supersonic points (dashed line), which match predictions from [22,53], indicating that the viscous scale is the engine for growth in the kinematic regime.

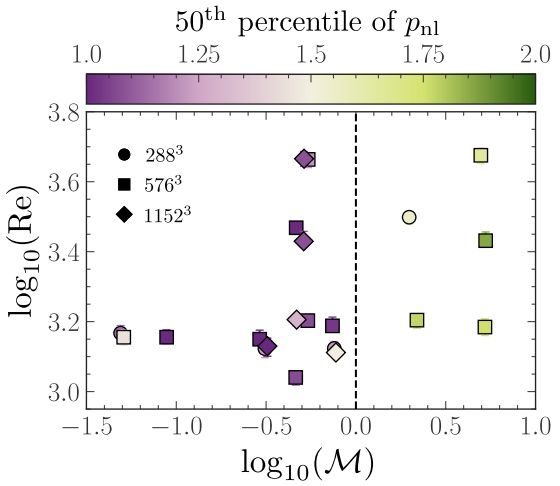

FIG. 3. Secular dynamo growth exponent $p_{\rm nl}$, measured during the nonlinear phase, as a function of $\mathcal{M}$ and Re for each plasma configuration. For $\mathcal{M} \lesssim 1$ simulations we unanimously recover linear growth [$p_{\rm nl} \approx 1$ (purple)], and quadratic growth [$p_{\rm nl} \approx 2$ (green)] for all $\mathcal{M} > 1$ simulations.

$\mathcal{M} > 1$ simulations. These fits indicate that the kinematic dynamo only converts approximately 1/100 of the hydrodynamical energy flux ε into magnetic energy. We show in the next section that this same conversion efficiency also holds in the nonlinear dynamo phase. These values are significantly smaller than predicted for Pm $\gg 1$ flows (37/36 for Kolmogorov flows and 11/60 for Burgers [22,53]) and instead align more closely with predictions for Pm $\ll 1$ flows, where 0.03 is expected for Kolmogorov flows and 5×10^{-3} for Burgers [22,53,54].

B. Nonlinear dynamo growth

Figure 3 shows our measured growth exponent $p_{\rm nl}$ for $E_{\rm mag}$ during the nonlinear phase, and Fig. 4 shows both the growth-efficiency coefficient $\alpha_{\rm nl}$[Fig. 4(a)] and duration $t_{\rm sat} - t_{\rm nl}$ of the nonlinear phase [Fig. 4(b)]. For our $\mathcal{M} \lesssim 1$ simulations, we find that growth is close to linear in time, $p_{\rm nl} \approx 1$, and a least-squares fit to the median results shows that the growth coefficient is $\alpha_{\rm nl} = (9.4 \pm 0.7) \times 10^{-3} \mathcal{M}^3 \approx 5 \times 10^{-3} \varepsilon$, where $\varepsilon \sim u_0^3/\ell_0 = 2\mathcal{M}^3$ is the hydrodynamic energy flux in our simulations. Critically, the growth rate is independent of Re, suggesting that, even though we have explored only a finite range Re $\in [10^3, 5 \times 10^3]$, the results are likely to be valid for all turbulent flows (where Re $>$ $\rm Re_{crit} \approx 100$; see Ref. [26]). This is qualitatively consistent with previous works that have shown only a small fixed fraction of ε is converted into magnetic energy [33,34], but it has never been measured with this accuracy and precision across a broad range of plasma parameters. By comparison, Beresnyak [33] measured $\alpha_{\rm nl}/\varepsilon \approx 0.05$ [compared to our $(9.4 \pm 0.7) \times 10^{-3}$–$10^{-2}$] from ensemble averaged $\mathcal{M} \ll 1$, Pm $= 1$ simulations, and Xu and Lazarian [37] predicted $\alpha_{\rm nl}/\varepsilon = 3/38$ for $\mathcal{M} \ll 1$, Pm $\gg 1$ SSDs. We show both of these predictions in Fig. 4, and while our measured efficiency is a factor of approximately 10 lower than both predictions, as was also the case for the growth rate measured during the kinematic phase, the

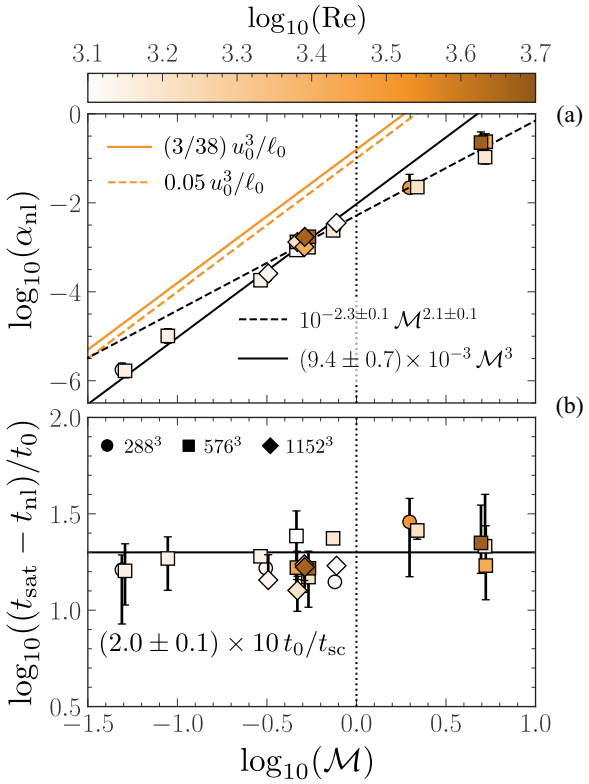

FIG. 4. (a) Nonlinear growth coefficient $\alpha_{\rm nl}$ and (b) duration of the nonlinear phase normalized by t_0, as a function of $\mathcal{M}$, and colored by Re. Points show median posterior values as derived from the MCMC, while error bars show the 16th to 84th percentile range, although in some cases the error bars are not visible because they are smaller than the plot markers. For $\mathcal{M} \lesssim 1$ we find $\alpha_{\rm nl} \propto \mathcal{M}^3$ (black solid line), consistent with turbulent energy-flux-regulated models of nonlinear growth: $0.05 u_0^3/\ell_0$ from [33] (orange dot-dashed line) and $(3/38) u_0^3/\ell_0$ from [37] (orange dotted line). By contrast, for $\mathcal{M} > 1$, we find $\alpha_{\rm nl} \propto \mathcal{M}^2$ (black dashed line), which is shallower than the flux-regulated prediction. Critically, $\alpha_{\rm nl}$ in both $\mathcal{M}$ regimes becomes independent of Re, and the cascade itself becomes the dynamo engine, where we find that only a roughly constant fraction of the turbulent kinetic energy flux is converted into magnetic energy, viz., $(dE_{\rm mag}/dt)/\varepsilon \approx 1/100$. Across all simulations the nonlinear phase persists for a universal $t_{\rm sat} - t_{\rm nl} \approx 20 t_0$ [black solid line in (b)] duration, invariant to all plasma parameters explored in this study.

difference, at least compared with Xu and Lazarian [37], can be explained by our finite Pm $= 1$ simulations. Regardless, the overall results are consistent with the phenomenology of inefficient conversion of turbulent to magnetic energy in the nonlinear phase.

All of our $\mathcal{M} > 1$ simulations yield $p_{\rm nl} \approx 2$, consistent with quadratic-in-time growth [55] of $E_{\rm mag}$, aligned with the model of Schleicher *et al.* [40], which predicts that $E_{\rm mag}(t) \sim E_{\rm kin}^{1/2}(t/t_0)^2$ for Burgers-like turbulence. Indeed, as predicted by Schleicher *et al.* [40], this breaks the universality of $p_{\rm nl}$ across different $\mathcal{M}$ regimes. Moreover, unlike the subsonic case, ε no longer scales with $\mathcal{M}^3$, but instead follows a shallower trend $\alpha_{\rm nl} \propto \varepsilon \propto \mathcal{M}^2$. Empirically, the trends we measure can be understood if the conversion of $E_{\rm kin}$ into $E_{\rm mag}$ is modified by the presence of acoustic modes and shocks,

i.e., if the flux is transferred on t_{sc} timescales, due to a fraction of the energy being directly deposited into shock heating, $\varepsilon \sim u^2/t_{sc} \sim u^2 c_s/\ell \sim \mathcal{M}^2$, which acts to reduce the available hydrodynamical flux by a factor of $\mathcal{M}^{-1}$. This is consistent with the idea that in the compressible regime, some fraction of the E_{kin} fills compressible mode degrees of freedom, which do not contribute to irreversible field amplification [28,31,32,46,56].

Despite the differences in scaling and $\mathcal{M}$ dependence between the $\mathcal{M} \lesssim 1$ and $\mathcal{M} > 1$ regimes, we find two aspects of the nonlinear SSD that are universal across plasma parameters and $\mathcal{M}$ regimes. First, the proportionality coefficient, which is associated with the nonlinear SSD efficiency, is universal across all $\mathcal{M}$ and Re, with $\varepsilon/100$ efficiency consistent with what was found previously [33], even though p_{nl} is not always unity. Second, across the full parameter space, we find that the nonlinear phase persists for $t_{sat} - t_{nl} \approx (20 \pm 1)t_0$, independent of $\mathcal{M}$ or Re [see Fig. 4(b)], making the duration in the nonlinear dynamo also universal. This suggests that once the nonlinear phase begins, $E_{mag} \approx E_{kin}(\ell_\nu)$, the system saturates after approximately $20t_0$, regardless of flow compressibility. This universal nonlinear window is visually apparent in both Fig. 1(b) and the inset in Fig. 1(a), where the nonlinear phase occupies a comparable interval when time is expressed as t/t_0 or $\log_{10}(t/t_{sc})$. This is likely because, although ε and α_{nl} have different $\mathcal{M}$ dependences, their ratio remains $\alpha_{nl}/\varepsilon \approx 1/100$ for all dynamo (both kinematic and nonlinear) and flow regimes (sub- and supersonic) [Fig. 4(a)]. The implication is that while the algebraic order and $\mathcal{M}$ dependence of E_{mag} growth depend on the turbulent regime, the path to saturation is set by a robust and universal dynamical clock.

IV. CONCLUSION

In this study we presented a detailed statistical analysis of small-scale dynamo growth across a range of hydrodynamic Reynolds Re and sonic Mach numbers $\mathcal{M}$, focusing on the poorly explored nonlinear phase of field growth. In order to access this regime, we (i) simulated many statistical realizations of each set of plasma parameters, allowing our measurements to become less sensitive to large statistical fluctuations that make this phase challenging to explore, and (ii) used a hierarchical Bayesian model fitting technique that allowed us to precisely model the dynamo phase transitions. We found that in this regime the growth rate depends on $\mathcal{M}$, but is liberated from any viscoresistive dynamics. The $\mathcal{M} < 1$ nonlinear SSDs grow proportionally to t with an efficiency of order of approximately $1/100$ of the hydrodynamic energy flux from the turbulence cascade, consistent with the phenomenological models with the incompressible nonlinear SSD [19,37]. Further, $\mathcal{M} > 1$ dynamos grow proportionally to t^2, predicted by existing theories [22,40], and with the same SSD efficiency approximately equal to $1/100$, making both the sub- and supersonic nonlinear dynamos universally inefficient in their parasitism of the hydrodynamical cascade [33].

Following from the universal efficiency, we found that the nonlinear phase has an approximately universal duration of approximately $20t_0$, where t_0 is the outer-scale turbulence turnover time, independent of both the Re and $\mathcal{M}$. Consequently, the time it takes systems to evolve through the nonlinear phase and reach E_{mag} saturation is always roughly an order of magnitude longer than the time it takes systems to reach mechanical equilibrium approximately equal to t_0, but no more. This implies that most observed astrophysical systems, which persist for many t_0, are likely to have reached SSD saturation; only those that have undergone large perturbations very recently or that are very dynamically young are likely to be in the nonlinear phase. Why the efficiency of the nonlinear SSD is approxiately $1/100$ and the characteristic duration of the phase approximately equal to $20t_0$, rather than any other values, remains an open theoretical question.

We note that our study has focused on Pm $= 1$ plasmas, while many hot astrophysical plasmas are Pm $\gg 1$ (Pm $\propto T^4/n_e$, where T is the plasma temperature and n_e is the electron number density). Our choice of Pm $= 1$ was motivated by the fact that in this study we targeted the nonlinear phase that begins once $E_{mag} \approx E_{kin}$ on the viscous scale and the backreaction that operates on dynamically important (viscous and larger) scales. In Pm $\gg 1$ systems, theory predicts that the nonlinear phase studied here may be preceded by another nonlinear, secular dynamo phase, where the magnetic field traverses the subviscous range of scales before reaching the viscous scale [19]. Our results therefore provide a useful anchor for future studies that explore this earlier stage of nonlinear evolution.

Finally, we note that our $\mathcal{M} > 1$ simulations do not resolve a $u_{\ell_s} = c_s$ sonic scale, where the velocity spectrum transitions between a subsonic and supersonic cascade [29,39]. It may be that the nonlinear SSD transitions smoothly between the $E_{mag} \sim \mathcal{M}^3 t$ and $E_{mag} \sim \mathcal{M}^2 t^2$ growth phase, as in Fig. 4, which may be relevant for $\mathcal{M} \gg 1$, Re $\gg 1$ astrophysical plasmas. We leave the study of this regime for future, extremely high-resolution nonlinear SSD investigations.

ACKNOWLEDGMENTS

We are deeply grateful to Christoph Federrath for allowing us to use his version of the FLASH code [39,45], which enabled this project. We also thank Tomasz Rozanski and Cameron Van Eck for many helpful discussions surrounding our Bayesian analysis. N.K. and M.R.K. acknowledge support from the Australian Research Council through Laureate Fellowship Award No. FL220100020. This research was undertaken with the assistance of resources from the National Computational Infrastructure (Australia), an NCRIS enabled capability supported by the Australian Government, through Award No. jh2. J.R.B. acknowledges funding from the Natural Sciences and Engineering Research Council of Canada (Reference No. 568580), support from NSF Award No. 2206756, and high-performance computing resources provided by the Leibniz Rechenzentrum and the Gauss Center for Supercomputing (Grants No. pn76gi, No. pr73fi, and No. pn76ga).

DATA AVAILABILITY

The data that support the findings of this article are openly available [52].

APPENDIX A: SIMULATION SETUP

For all simulations we solve the compressible set of nonideal (viscoresistive) magnetohydrodynamical fluid equations

$$\frac{\partial \rho}{\partial t} + \nabla \cdot (\rho \boldsymbol{u}) = 0, \tag{A1}$$

$$\frac{\partial \rho \boldsymbol{u}}{\partial t} + \nabla \cdot \left[\rho \boldsymbol{u} \otimes \boldsymbol{u} - \frac{1}{4\pi} \boldsymbol{b} \otimes \boldsymbol{b} + \left(c_s^2 \rho + \frac{b^2}{8\pi} \right) \overleftrightarrow{\boldsymbol{I}} - 2\nu\rho \overleftrightarrow{\boldsymbol{S}} \right] = \rho \boldsymbol{f}, \tag{A2}$$

$$\frac{\partial \boldsymbol{b}}{\partial t} + \nabla \cdot (\boldsymbol{u} \otimes \boldsymbol{b} - \boldsymbol{b} \otimes \boldsymbol{u}) = \eta \nabla^2 \boldsymbol{b}, \tag{A3}$$

$$\nabla \cdot \boldsymbol{b} = 0, \tag{A4}$$

where ρ is gas density, $\boldsymbol{u}$ is the gas velocity, $\boldsymbol{b}$ is the magnetic field, c_s is sound speed, ν is the kinematic viscosity, η is the magnetic resistivity, and $\overleftrightarrow{\boldsymbol{I}} = \delta^i_j$ is the identity tensor. We model our viscosity via the traceless strain rate tensor

$$\overleftrightarrow{\boldsymbol{S}} = \tfrac{1}{2}[\nabla \otimes \boldsymbol{u} + (\nabla \otimes \boldsymbol{u})^T] - \tfrac{1}{3}(\nabla \cdot \boldsymbol{u}) \overleftrightarrow{\boldsymbol{I}}, \tag{A5}$$

where $\otimes$ is the tensor product $\nabla \otimes \boldsymbol{u} \equiv \partial^i u_j$. Our simulations span a broad range of $\mathcal{M}$ and Re and are run at a range of resolutions; see Sec. II A for details and Table I for a full list. The forcing function $\boldsymbol{f}$ is Gaussian random and the phases are evolved in time using the TURBGEN implementation [45] of an Ornstein-Uhlenbeck process, where the correlation time sets to the outer scale of the turbulence t_0. We set the injection to peak on $\ell_0 = L/2$ and tune the forcing amplitude so that the velocity field on ℓ_0 stays within 5% of a chosen target value during the kinematic phase; we explore $\mathcal{M} \in [5 \times 10^{-2}, 5]$.

APPENDIX B: MCMC PARAMETERS

We carried out all fits using the `emcee` ensemble sampler [51]. For each parameter vector we employed ten walkers per free parameter, each evolved for 10^4 steps, where the first 3×10^3 steps were discarded as burn-in, with no thinning applied. In the first stage, walkers were initialized with small, 1% Gaussian scatter around the prior ranges, while in the second stage we initialized them with a 1% Gaussian scatter relative to the median parameters inferred from stage 1. Convergence was verified by monitoring the integrated autocorrelation time of the chains, by inspecting the stability of the posterior distributions, and by checking that the median acceptance fraction across walkers lies within the recommended range of 0.2–0.5. As discussed in the main text, all posteriors are based on the combined post-burn-in samples, and the measurements reported are of percentiles over the combined ensembles.

APPENDIX C: MODEL COMPARISON WITH AKAIKE INFORMATION CRITERION

To further test the robustness of our inference, we employed the Akaike information criterion (AIC). For each dataset i and candidate model $j \in \mathcal{N} \equiv \{p_{\rm nl} = 1,\ p_{\rm nl} = 2\}$, we calculate

$$\mathrm{AIC}_{ij} = 2k - 2 \ln \mathcal{L}(d_i \mid \hat{\boldsymbol{\theta}}_j), \tag{C1}$$

where d_i denotes a unique plasma configuration instance, $\hat{\boldsymbol{\theta}}_j$ are the maximum-likelihood parameters for model j, and $k = 5$ is the number of free parameters (which is the same for both models). Model comparison is then based on the relative AIC weights

$$w_{ij} = \frac{\exp\left(-\frac{1}{2}\Delta_{ij}\right)}{\sum_{n \in \mathcal{N}} \exp\left(-\frac{1}{2}\Delta_{in}\right)}, \tag{C2}$$

with

$$\Delta_{ij} = \mathrm{AIC}_{ij} - \min_{n \in \mathcal{N}} \mathrm{AIC}_{in}. \tag{C3}$$

The weights w_{ij} quantify the probability that model j is preferred for dataset i. In practice, for many datasets the weight of the favored model is numerically $w \approx 1$, while the alternative has $w \approx 0$ (to machine precision). This outcome is expected when the number of independent data points is large and gives us confidence that the nonlinear phase has been sufficiently resolved to independently constrain the dynamics in this transitionary regime.

Among the $\mathcal{M} \lesssim 1$ simulations we find that most cases ($19/30 \approx 63\%$) favor the linear model ($p_{\rm nl} = 1$), while the quadratic model ($p_{\rm nl} = 2$) is preferred ($29/40 \approx 73\%$) by the $\mathcal{M} > 1$ simulations. These findings independently confirm the dichotomy in nonlinear growth behavior shown in Figs. 3 and 4, and the relative fractions are consistent with those inferred from our MCMC fits within their statistical uncertainties.

[1] A. Brandenburg, D. Sokoloff, and K. Subramanian, Current status of turbulent dynamo theory: From large-scale to small-scale dynamos, Space Sci. Rev. **169**, 123 (2012).

[2] F. Rincon, Dynamo theories, J. Plasma Phys. **85**, 205850401 (2019).

[3] M. Rempel, T. Bhatia, L. Bellot Rubio, and M. J. Korpi-Lagg, Small-scale dynamos: From idealized models to solar and stellar applications, Space Sci. Rev. **219**, 36 (2023).

[4] S. Roh, D. Ryu, H. Kang, S. Ha, and H. Jang, Turbulence dynamo in the stratified medium of galaxy clusters, Astrophys. J. **883**, 138 (2019).

[5] L. Tevlin, T. Berlok, C. Pfrommer, R. Y. Talbot, J. Whittingham, E. Puchwein, R. Pakmor, R. Weinberger, and V. Springel, Magnetic dynamos in galaxy clusters: The crucial role of galaxy formation physics at high redshifts, Astron. Astrophys. **701**, A114 (2025).

[6] J. Whittingham, M. Sparre, C. Pfrommer, and R. Pakmor, The impact of magnetic fields on cosmological galaxy mergers–I. Reshaping gas and stellar discs, Mon. Not. R. Astron. Soc. **506**, 229 (2021).

[7] C. Palenzuela, R. Aguilera-Miret, F. Carrasco, R. Ciolfi, J. V. Kalinani, W. Kastaun, B. Miñano, and D. Viganò, Turbulent magnetic field amplification in binary neutron star mergers, Phys. Rev. D **106**, 023013 (2022).

[8] T. Ryu, A. Sills, R. Pakmor, S. de Mink, and R. Mathieu, Magnetic field amplification during stellar collisions

between low-mass stars, Astrophys. J. Lett. **980**, L38 (2025).

[9] P. Kempski, D. B. Fielding, E. Quataert, A. K. Galishnikova, M. W. Kunz, A. A. Philippov, and B. Ripperda, Cosmic ray transport in large-amplitude turbulence with small-scale field reversals, Mon. Not. R. Astron. Soc. **525**, 4985 (2023).

[10] M. Lemoine, Particle transport through localized interactions with sharp magnetic field bends in MHD turbulence, J. Plasma Phys. **89**, 175890501 (2023).

[11] Z. Vörös, O. W. Roberts, Y. Narita, E. Yordanova, R. Nakamura, A. Settino, D. Schmid, M. Volwerk, C. L. S. Wedlund, A. Varsani, L. Sorriso-Valvo, P. A. Bourdin, and Á. Kis, Turbulent dynamo in the terrestrial magnetosheath, Nat. Commun. **17**, 2909 (2026).

[12] J. Meinecke, H. W. Doyle, F. Miniati, A. R. Bell, R. Bingham, R. Crowston, R. P. Drake, M. Fatenejad, M. Koenig, Y. Kuramitsu, C. C. Kuranz, D. Q. Lamb, D. Lee, M. J. MacDonald, C. D. Murphy, H. S. Park, A. Pelka, A. Ravasio, Y. Sakawa, A. A. Schekochihin, *et al.*, Turbulent amplification of magnetic fields in laboratory laser-produced shock waves, Nat. Phys. **10**, 520 (2014).

[13] P. Tzeferacos, A. Rigby, A. Bott, A. Bell, R. Bingham, A. Casner, F. Cattaneo, E. Churazov, J. Emig, F. Fiuza, *et al.*, Laboratory evidence of dynamo amplification of magnetic fields in a turbulent plasma, Nat. Commun. **9**, 591 (2018).

[14] A. F. A. Bott, L. Chen, G. Boutoux, T. Caillaud, A. Duval, M. Koenig, B. Khiar, I. Lantuéjoul, L. Le-Deroff, B. Reville, R. Rosch, D. Ryu, C. Spindloe, B. Vauzour, B. Villette, A. A. Schekochihin, D. Q. Lamb, P. Tzeferacos, G. Gregori, and A. Casner, Inefficient magnetic-field amplification in supersonic laser-plasma turbulence, Phys. Rev. Lett. **127**, 175002 (2021).

[15] A. F. A. Bott, P. Tzeferacos, L. Chen, C. A. J. Palmer, A. Rigby, A. R. Bell, R. Bingham, A. Birkel, C. Graziani, D. H. Froula, J. Katz, M. Koenig, M. W. Kunz, C. Li, J. Meinecke, F. Miniati, R. Petrasso, H.-S. Park, B. A. Remington, B. Reville, *et al.*, Time-resolved turbulent dynamo in a laser plasma, Proc. Natl. Acad. Sci. USA **118**, e2015729118 (2021).

[16] H. Moffatt, Dynamo action associated with random inertial waves in a rotating conducting fluid, J. Fluid Mech. **44**, 705 (1970).

[17] S. I. Vainshtein and Y. B. Zel'dovich, Origin of magnetic fields in astrophysics (turbulent "dynamo" mechanisms), Sov. Phys. Usp. **15**, 159 (1972).

[18] R. M. Kulsrud and S. W. Anderson, The spectrum of random magnetic fields in the mean field dynamo theory of the galactic magnetic field, Astrophys. J. **396**, 606 (1992).

[19] A. A. Schekochihin, S. C. Cowley, G. Hammett, J. Maron, and J. McWilliams, A model of nonlinear evolution and saturation of the turbulent MHD dynamo, New J. Phys. **4**, 84 (2002).

[20] A. A. Schekochihin, S. C. Cowley, S. F. Taylor, J. L. Maron, and J. C. McWilliams, Simulations of the small-scale turbulent dynamo, Astrophys. J. **612**, 276 (2004).

[21] J. Maron, S. Cowley, and J. McWilliams, The nonlinear magnetic cascade, Astrophys. J. **603**, 569 (2004).

[22] J. Schober, D. Schleicher, C. Federrath, R. Klessen, and R. Banerjee, Magnetic field amplification by small-scale dynamo action: Dependence on turbulence models and Reynolds and Prandtl numbers, Phys. Rev. E **85**, 026303 (2012).

[23] X. Bian and H. Aluie, Decoupled cascades of kinetic and magnetic energy in magnetohydrodynamic turbulence, Phys. Rev. Lett. **122**, 135101 (2019).

[24] A. Brandenburg and M. Rempel, Reversed dynamo at small scales and large magnetic Prandtl number, Astrophys. J. **879**, 57 (2019).

[25] P. Grete, B. W. O'Shea, and K. Beckwith, As a matter of tension: Kinetic energy spectra in MHD turbulence, Astrophys. J. **909**, 148 (2021).

[26] N. Kriel, J. R. Beattie, A. Seta, and C. Federrath, Fundamental scales in the kinematic phase of the turbulent dynamo, Mon. Not. R. Astron. Soc. **513**, 2457 (2022).

[27] N. Kriel, J. R. Beattie, C. Federrath, M. R. Krumholz, and J. K. J. Hew, Fundamental MHD scales–II. The kinematic phase of the supersonic small-scale dynamo, Mon. Not. R. Astron. Soc. **537**, 2602 (2025).

[28] J. R. Beattie, C. Federrath, N. Kriel, J. K. J. Hew, and A. Bhattacharjee, Taking control of compressible modes: Bulk viscosity and the turbulent dynamo, Mon. Not. R. Astron. Soc. **542**, 2669 (2025).

[29] J. R. Beattie, C. Federrath, R. S. Klessen, S. Cielo, and A. Bhattacharjee, The spectrum of magnetized turbulence in the interstellar medium, Nat. Astron. **9**, 1195 (2025).

[30] A. P. Kazantsev, Enhancement of a magnetic field by a conducting fluid, Sov. Phys. JETP **26**, 1031 (1968).

[31] C. Federrath, G. Chabrier, J. Schober, R. Banerjee, R. S. Klessen, and D. R. G. Schleicher, Mach number dependence of turbulent magnetic field amplification: Solenoidal versus compressive flows, Phys. Rev. Lett. **107**, 114504 (2011).

[32] C. Federrath, J. Schober, S. Bovino, and D. R. G. Schleicher, The turbulent dynamo in highly compressible supersonic plasmas, Astrophys. J. Lett **797**, L19 (2014).

[33] A. Beresnyak, Universal nonlinear small-scale dynamo, Phys. Rev. Lett. **108**, 035002 (2012).

[34] J. Cho, E. T. Vishniac, A. Beresnyak, A. Lazarian, and D. Ryu, Growth of magnetic fields induced by turbulent motions, Astrophys. J. **693**, 1449 (2009).

[35] A. Seta and C. Federrath, Seed magnetic fields in turbulent small-scale dynamos, Mon. Not. R. Astron. Soc. **499**, 2076 (2020).

[36] A. K. Galishnikova, M. W. Kunz, and A. A. Schekochihin, Tearing instability and current-sheet disruption in the turbulent dynamo, Phys. Rev. X **12**, 041027 (2022).

[37] S. Xu and A. Lazarian, Turbulent dynamo in a conducting fluid and a partially ionized gas, Astrophys. J. **833**, 215 (2016).

[38] C. Federrath, On the universality of supersonic turbulence, Mon. Not. R. Astron. Soc. **436**, 1245 (2013).

[39] C. Federrath, R. S. Klessen, L. Iapichino, and J. R. Beattie, The sonic scale of interstellar turbulence, Nat. Astron. **5**, 365 (2021).

[40] D. R. Schleicher, J. Schober, C. Federrath, S. Bovino, and W. Schmidt, The small-scale dynamo: Breaking universality at high Mach numbers, New J. Phys. **15**, 023017 (2013).

[41] J. Schober, D. R. G. Schleicher, C. Federrath, S. Bovino, and R. S. Klessen, Saturation of the turbulent dynamo, Phys. Rev. E **92**, 023010 (2015).

[42] B. Fryxell, K. Olson, P. Ricker, F. X. Timmes, M. Zingale, D. Q. Lamb, P. MacNeice, R. Rosner, J. W. Truran, and H. Tufo, FLASH: An adaptive mesh hydrodynamics code for modeling astrophysical thermonuclear flashes, Astrophys. J. Suppl. **131**, 273 (2000).

[43] A. Dubey, R. Fisher, C. Graziani, G. C. Jordan, IV, D. Q. Lamb, L. B. Reid, P. Rich, D. Sheeler, D. Townsley, and K. Weide, in *Numerical Modeling of Space Plasma Flows*, edited by N. V. Pogorelov, E. Audit, and G. P. Zank, Astronomical Society of the Pacific Conference Series (Astronomical Society of the Pacific, San Francisco, 2008), Vol. 385, p. 145.

[44] K. Waagan, C. Federrath, and C. Klingenberg, A robust numerical scheme for highly compressible magnetohydrodynamics: Nonlinear stability, implementation and tests, J. Comput. Phys. **230**, 3331 (2011).

[45] C. Federrath, J. Roman-Duval, R. S. Klessen, W. Schmidt, and M.-M. Mac Low, TG: Turbulence Generator, Astrophysics Source Code Library, record ascl:2204.001 (2022).

[46] A. Seta and C. Federrath, Saturation mechanism of the fluctuation dynamo in supersonic turbulent plasmas, Phys. Rev. Fluids **6**, 103701 (2021).

[47] L. M. Shivakumar and C. Federrath, Numerical viscosity and resistivity in MHD turbulence simulations, Mon. Not. R. Astron. Soc. **537**, 2961 (2025).

[48] A. Schekochihin, A. Iskakov, S. Cowley, J. McWilliams, M. Proctor, and T. Yousef, Fluctuation dynamo and turbulent induction at low magnetic Prandtl numbers, New J. Phys. **9**, 300 (2007).

[49] A. Seta, P. J. Bushby, A. Shukurov, and T. S. Wood, Saturation mechanism of the fluctuation dynamo at $\mathrm{Pr}_M \geqslant 1$, Phys. Rev. Fluids **5**, 043702 (2020).

[50] A. Brandenburg, I. Rogachevskii, and J. Schober, Dissipative magnetic structures and scales in small-scale dynamos, Mon. Not. R. Astron. Soc. **518**, 6367 (2022).

[51] D. Foreman-Mackey, D. W. Hogg, D. Lang, and J. Goodman, emcee: The MCMC hammer, Publ. Astron. Soc. Pac. **125**, 306 (2013).

[52] N. Kriel, Data and analysis scripts for "Universal growth of magnetic energy during the nonlinear phase of subsonic and supersonic small-scale dynamos" (GitHub, San Francisco, 2025), https://github.com/AstroKriel/Kriel2025_ssd_nl/.

[53] J. Schober, D. Schleicher, S. Bovino, and R. S. Klessen, Small-scale dynamo at low magnetic Prandtl numbers, Phys. Rev. E **86**, 066412 (2012).

[54] S. Bovino, D. R. Schleicher, and J. Schober, Turbulent magnetic field amplification from the smallest to the largest magnetic Prandtl numbers, New J. Phys. **15**, 013055 (2013).

[55] A complementary model-comparison analysis (see Appendix C) confirms that subsonic results are best described by linear growth, while quadratic growth captures the supersonic regime.

[56] S. Sur and K. Subramanian, Role of magnetic pressure forces in fluctuation dynamo saturation, Mon. Not. R. Astron. Soc. **527**, 3968 (2023).